Spin-orbit driven ferromagnetic resonance

D. Fang[1], H. Kurebayashi[1], J. Wunderlich[2,3], K. Výborný[2,4], L. P. Zârbo[2], R. P. Campion[5], A. Casiraghi[5], B. L. Gallagher[5], T. Jungwirth[2,5] & A. J. Ferguson[1*]

[1] *Microelectronics Group, Cavendish Laboratory, University of Cambridge, JJ Thomson Avenue, Cambridge CB3 0HE, UK*

[2] *Institute of Physics ASCR, v.v.i., Cukrovarnická 10, 162 53 Praha 6, Czech Republic*

[3] *Hitachi Cambridge Laboratory, Cambridge CB3 0HE, UK*

[4] *Present address: Department of Physics, State University of New York at Buffalo, Buffalo, New York 14260, USA*

[5] *School of Physics and Astronomy, University of Nottingham, Nottingham NG7 2RD, UK*

Ferromagnetic resonance (FMR) is the most widely used technique for characterising ferromagnets.[1] In specific non-uniform magnetic micro-devices such as spin-valves, it was demonstrated that FMR can be directly induced by an alternating current.[2,3] The technique uses the spin-transfer torque[4] which can be viewed as a macroscopic angular momentum transfer effect. We introduce a form of FMR induced by driving an alternating current through a uniformly magnetised nanomagnet. The method relies on a microscopic non-collinearity of individual electron spins due to the spin-orbit (SO) coupling and bulk or structural inversion asymmetry in the band structure of the sample. The SO induced driving field in uniform magnets has been previously utilised for magnetisation switching in the ferromagnetic semiconductor (Ga,Mn)As[5] and for domain nucleation in a Pt/Co/AlO_x stack.[6] We perform vector magne-

tometry on the driving field showing contributions with the symmetry of both the Dresselhaus and Rashba SO interactions. Using our SO-FMR, we perform broadband measurements of micromagnetic parameters of lithographically patterned (Ga,Mn)As and (Ga,Mn)(As,P) nano-bars.

The principle of the SO-FMR technique is illustrated in Figure 1a. When an alternating electrical current traverses through the uniformly magnetised material, the resulting non-equilibrium distribution of occupied states in the SO-coupled carrier bands yields a non-equilibrium time-dependent spin polarisation.[7–10] The polarisation produces a transverse component of the internal exchange field and a torque is applied which drives the precession of the magnetisation vector.[11,12]

The micro and nano-bars employed in our study are patterned from 25 nm-thick films of $(Ga_{0.94},Mn_{0.06})As$ and $(Ga_{0.94},Mn_{0.06})(As_{0.9},P_{0.1})$. To drive the FMR we pass a microwave-frequency current through the nano-bar (Figure 1b). For detection we utilise a frequency mixing effect based on the anisotropic magnetoresistance (AMR).[13–18] When the magnetisation precession is driven, a time-dependent change $\Delta R(t)$ in the longitudinal resistance from the equilibrium value R occurs (due to the AMR). The resistance oscillates with the same frequency as the microwave current, therefore causing frequency mixing and a directly measurable dc voltage, V_{dc}, is generated. This voltage provides a direct probe of the amplitude and phase of the magnetisation precession with respect to the microwave current.

We first show measurements on a 80 nm-wide nano-bar patterned in the $[1\bar{1}0]$ direction from the (Ga,Mn)(As,P) epilayer. The magnetic field dependence of V_{dc} is measured at different mi-

crowave frequencies and taken at a temperature of 6 K. The frequency of the incident current is fixed while an external dc magnetic field $\mathbf{H}_0$ is swept and a well-defined resonance peak appears (Figure 2a). The peak is well-fitted by the solution of the Landau-Lifshitz-Gilbert (LLG) equation, which describes the dynamics of precessional motion of the magnetisation. The resonance lineshape is a combination of symmetric and anti-symmetric Lorentzian functions with amplitudes V_{sym} and V_{asy}, respectively.

Figure 2b plots the frequency-dependence of the resonance field H_{res} which fits well to a modified Kittel formula (see Equation 3 in Methods). The FMR linewidth ($\Delta H = \Delta H_{\text{inhomo}} + \alpha\omega/\gamma$) describes the damping in the ferromagnetic system. The broadband nature of our setup allows us to determine the inhomogeneous (2.5 mT) and frequency-dependent contributions to the damping (Figure 2c) corresponding to a Gilbert-damping constant of $\alpha = 0.023$. Using a vector field cryostat we also perform the SO-FMR measurements for different orientations of the external magnetic field. In Figure 2d we present the data from an in-plane scan of the magnetic field showing that there is a strong uniaxial anisotropy perpendicular to the bar direction. By analysing the peak positions (Figure 2e) using Equation 3 we quantify the anisotropy fields and find $\mu_0 H_{2\parallel} = -180$ mT (uniaxial) and $\mu_0 H_{4\parallel} = 68$ mT (biaxial). As well as the FMR signal, we also note the presence of a non-resonant, angle dependent background signal (Figure 2d) due to a bolometric or thermoelectric effect.

To characterise SO-FMR we must understand the direction and amplitude of the effective field $\mathbf{h}_{\text{eff}}$ that drives magnetisation precession. We are able to perform vector magnetometry on

the driving field from the angle dependence of the amplitude of the FMR peak.[2,3] For a vector driving field $\mathbf{h}_{\text{eff}}(t) = (h_x, h_y, h_z)e^{i\omega t}$ in-phase with the microwave current $\mathbf{I}(t) = (I, 0, 0)e^{i\omega t}$, the amplitudes of the two components of the FMR peak are (see Supplementary Information for derivation):

$$V_{\text{sym}}(\theta) = \frac{I\Delta R}{2} A_{\text{sym}} \sin(2\theta) h_z \tag{1}$$

$$V_{\text{asy}}(\theta) = \frac{I\Delta R}{2} A_{\text{asy}} \sin(2\theta)(h_x \sin\theta + h_y \cos\theta) \tag{2}$$

where ΔR is the non-crystalline AMR coefficient of the ferromagnetic sample, θ is the angle between the applied field $\mathbf{H}_0$ and the current $\mathbf{I}$, and $A_{\text{sym(asy)}}$ are constants determined by the magnetic anisotropies. Hence by decomposing the resonance lineshape into V_{sym} and V_{asy}, and by measurements of the AMR and magnetic anisotropies we are able to deduce the components of $\mathbf{h}_{\text{eff}}$. In the Supplementary Information we verify this vector magnetometry technique in a sample where the FMR is driven by the microwave magnetic field from a short-circuited waveguide.

No component of V_{sym} is seen to behave as $\sin(2\theta)$, indicating that the driving field $\mathbf{h}_{\text{eff}}$ is predominantly in-plane. Accordingly we restrict our discussion to V_{asy}, however a comparison of V_{asy} and V_{sym} is found in the Supplementary Information. Figure 3a shows the angle-dependence of V_{asy} for a 500 nm-wide (Ga,Mn)As bar patterned in the $[1\bar{1}0]$ direction. We see that $V_{\text{asy}}(\theta)$ comprises a $-\sin(2\theta)\cos(\theta)$ term, indicating that the driving field is perpendicular to $\mathbf{I}$. In a [110] device (Figure 3a) the amplitude of V_{asy} has the opposite sign, indicating that the driving field has reversed. For nano-bars along [100] and [010] (Figure 3b), the V_{asy} curve is a superposition of $\sin(2\theta)\sin(\theta)$ and $\sin(2\theta)\cos(\theta)$ functions, showing that the driving field consists of components

both parallel and perpendicular to $\mathbf{I}$.

These data are most clearly seen by plotting the dependence of the magnitude and direction of the effective field on the current (nano-bar) orientation (Figure 3c). Two contributions to the driving field are observed with different symmetry, $\mathbf{h}_{\text{eff}} = \mathbf{h}_{\text{D}} + \mathbf{h}_{\text{R}}$. Quantitative microscopic understanding of these contributions is provided by calculations which we describe in detail in the Supplementary Information. The theory links the SO-FMR driving fields to the inversion-symmetry breaking terms in the relativistic 3D Hamiltonian of the ferromagnetic semiconductor, $\mathcal{H}_{C4} = C_4 \sum_i J_i k_i (e_{i+1\,i+1} - e_{i+2\,i+2}) + C_4 \sum_i (J_i k_{i+1} - J_{i+1} k_i) e_{i\,i+1}$.[5,19] These terms originate from the combined effects of inversion asymmetry of the bulk zinc-blende lattice and uniform strain. Here $\mathbf{J}$ is the hole total angular momentum operator, $\mathbf{k}$ is the wavevector, $\mathbf{e}$ is the strain tensor, and $C_4 \sim 0.5$ eVnm for the GaAs semiconductor host. The first term in $\mathcal{H}_{C4}$, which yields $\mathbf{h}_{\text{D}}$, is present in our samples due to the substrate-ferromagnet lattice matching growth strain, $e_{xx} = e_{yy} \neq e_{zz}$. It depends only on the in-plane (x and y) components of the angular momentum and wavevector and, up to a prefactor, is identical to the Dresselhaus SO Hamiltonian of a 2D electron gas. As expected from the model, our experimental data (Figure 3c & d) show that $\mathbf{h}_{\text{D}}$ changes sign as the strain changes from compressive ((Ga,Mn)As) to tensile ((Ga,Mn)(As,P)). The second term in $\mathcal{H}_{C4}$ yields the observed $\mathbf{h}_{\text{R}}$ if it takes a form analogous to the 2D Rashba SO Hamiltonian, i.e. if $e_{xy} = e_{yx} \neq 0$. This shear strain is not physically present in the crystal structure of ferromagnetic semiconductor epilayers. It has been introduced, however, in previous studies to model the in-plane uniaxial anisotropy present in (Ga,Mn)As and the values of this effective off-diagonal strain are typically several times smaller than the diagonal, growth-induced strain.[20] This

is consistent with the observed smaller magnitude of $\mathbf{h}_\mathrm{R} = 6.5\ \mu$T than $\mathbf{h}_\mathrm{D} = 18\ \mu$T (values given at $j = 10^5$ A/cm^2). Furthermore, $\mathbf{h}_\mathrm{R}$ may contain a contribution from the Oersted field (discussed in the Supplementary Information). Both $\mathbf{h}_\mathrm{D}$ and $\mathbf{h}_\mathrm{R}$ are measured to be linear in current density (Figure 3e & f). This measurement was performed for bars in the [100] direction where it is possible to independently resolve contributions to $\mathbf{h}_\mathrm{R}$ and $\mathbf{h}_\mathrm{D}$. We observe a larger magnitude of $\mathbf{h}_\mathrm{D}$ at a given current density in the (Ga,Mn)(As,P) nano-bars. This is explained by the larger magnitude of the growth strain and larger resistivity (larger E at given j) of (Ga,Mn)(As,P) as compared to the (Ga,Mn)As film.[21]

We now demonstrate that SO-FMR can be applied to comparative investigations of nano-bars where the anisotropies differ from bulk values.[22–25] We first compare the effect of strain-relaxation between 500 nm bars under compressive ((Ga,Mn)As) and tensile ((Ga,Mn)(As,P)) growth strain. The in-plane anisotropies are studied; although (Ga,Mn)(As,P) is out-of-plane magnetised,[21] the applied field $\mathbf{H}_0$ brings the magnetisation into plane. In (Ga,Mn)As we observe an additional uniaxial contribution to the anisotropy ($\mu_0 H_U = 32$ mT) along the bar (Figure 4a & c) with a similar magnitude to previous reports.[22,24,25] By contrast in the (Ga,Mn)(As,P) nano-bar (Figure 4b & c) the sign of the uniaxial anisotropy ($\mu_0 H_U = -30.5$ mT) has reversed and the easy axis is now perpendicular to the bar. This can be understood in terms of the sign of the strain relaxation: these materials become magnetically easier in the direction of most compressive (least tensile) strain. So when the tensile strain of the (Ga,Mn)(As,P) nano-bar relaxes, it introduces an easy axis perpendicular to the bar. Furthermore we measure (Ga,Mn)(As,P) bars of different widths (Figure 4e) and observe a decrease in the strain-relaxation induced anisotropy from the 80 nm bar

($\mu_0 H_U = -270$ mT) to the 500 nm bar ($\mu_0 H_U = -30.5$ mT), and almost no effect of strain-relaxation in the 4 μm bar ($\mu_0 H_U = -10.5$ mT).

As well as being able to determine the patterning-induced change in anisotropy, we also compare the damping among the nano-bars of different sizes (Figure 4d). The frequency-dependent term (related to damping) increases for decreasing bar width: $\alpha = 0.004$ (4 μm-wide), 0.006 (500 nm) and 0.023 (80 nm). The significantly higher value of Gilbert damping at 80 nm compared with the 500 nm and 4 μm bars may be due to damage during the etching process. The frequency-independent term is relevant in the case of strain relaxation as it indicates the inhomogeneity of anisotropy fields within the bar itself. The intermediate case of 500 nm shows greater inhomogeneity $\Delta H_{\text{inhomo}} = 9.9$ mT than the 4 μm bar $\Delta H_{\text{inhomo}} = 5.4$ mT, explained by the increased variation in local anisotropy. By contrast, for 80 nm bar reduces to $\Delta H_{\text{inhomo}} = 2.5$ mT, indicative of a high degree of strain-relaxation. The values of α and ΔH_{inhomo} for the 4 μm bar are comparable to measurements on bulk material by conventional FMR.[26]

In conclusion, we perform variable-frequency FMR experiments on individual micro and nano-bars of uniform ferromagnetic semiconductors (Ga,Mn)As and (Ga,Mn)(As,P). The FMR is driven by a torque at microwave frequencies whose origin lies in the internal effective field (due to the SO-coupling and exchange interaction) of the probed ferromagnet. Our work demonstrates a new FMR technique applicable to the magnetic characterisation of uniform ferromagnetic nanostructures and to the study of the current-induced effective magnetic fields in SO-coupled ferromagnets.

Methods

Sample preparation The 25 nm-thick ($Ga_{0.94}$,$Mn_{0.06}$)As and ($Ga_{0.94}$,$Mn_{0.06}$)($As_{0.9}$,$P_{0.1}$) epilayers are grown by molecular beam epitaxy at 230ºC on semi-insulating GaAs substrates. The (Ga,Mn)As samples are subsequently annealed at 190ºC for 20 h in air, and reach Curie temperature $T_C \approx 130$ K. The (Ga,Mn)(As,P) samples are annealed at 180ºC for 48 h and have $T_C \approx 110$ K. The devices are defined on the wafers by 200 nm-wide isolation trenches (~ 150 nm-deep), which are patterned using electron beam lithography and reactive etching. Cr/Au (20/200 nm) ohmic contacts are thermally evaporated. Typical longitudinal resistance of 500 nm-wide bars is $R = 17$ kΩ and $R = 20$ kΩ for the ($Ga_{0.94}$,$Mn_{0.06}$)As and ($Ga_{0.94}$,$Mn_{0.06}$)($As_{0.9}$,$P_{0.1}$) samples, respectively. The contact resistance of the ($Ga_{0.94}$,$Mn_{0.06}$)As samples is $2R_c = 1.6$ kΩ with a similar value expected for the ($Ga_{0.94}$,$Mn_{0.06}$)($As_{0.9}$,$P_{0.1}$).

Measurement technique The sample is wire bonded between an open-circuit coplanar transmission line and a low-frequency connection which also provides a microwave ground. A lock-in technique is employed to improve the signal-to-noise ratio in our measurements: The microwave current is pulse-modulated and a lock-in amplifier is then referenced to the modulation frequency (987.6 Hz). The difference in dc voltage across the sample between the two states, $V = V(I_{\text{on}}) - V(I_{\text{off}})$, is measured.

Calculating the magnetic anisotropy The modified Kittel formula which relates the magnetic anisotropies and the resonance frequency is given as:[27]

$$\left(\frac{\omega}{\gamma}\right)^2 = \mu_0^2 (H_{\text{res}} + H'_{\text{ani}})(H_{\text{res}} + H''_{\text{ani}}) \qquad (3)$$

where $H^{'}_{\text{ani}}$ and $H^{''}_{\text{ani}}$ are terms containing the demagnetisation and anisotropy energies of the ferromagnet:

$$
\begin{aligned}
H^{'}_{\text{ani}} &= M_s - H_{2\perp} + \frac{H_{4\|}}{4}(3+\cos 4\varphi) + H_{2\|}\cos^2\left(\varphi + \frac{\pi}{4}\right) + H_U \sin^2\varphi \\
H^{''}_{\text{ani}} &= H_{4\|}\cos 4\varphi - H_{2\|}\sin 2\varphi - H_U \cos 2\varphi
\end{aligned} \tag{4}
$$

Here φ is the angle between the magnetisation vector $\mathbf{M}$ and the [100] crystal direction and M_s is the saturation magnetisation. $H_{2\perp}$ is the out-of-plane uniaxial anisotropy ($H_{2\perp} > 0$ for perpendicular-to-plane easy axis); $H_{4\|}$ and $H_{2\|}$ represent the in-plane biaxial and uniaxial anisotropy fields, respectively; and H_U models the strain-relaxation-induced uniaxial anisotropy[25] ($H_U > 0$ if its easy axis is along [010]). The anisotropy fields H_i are defined in terms of the anisotropy energy density K_i (with unit J/cm^3) according to $H_i = 2K_i/\mu_0 M_s$ and conform to the free energy definition in Eq. (1) of Ref. 27.

By fitting the $H_{\text{res}}(\varphi)$ data (Figure 2e; and Figure 4a, b & e), we are able to determine the in-plane anisotropy fields $H_{4\|}$, $H_{2\|}$ and H_U in our nano-devices. A gyromagnetic constant γ characteristic for Mn^{2+} spins of 176 GHz/T (g-factor 2) is used for the fittings.

Note that the above equations are derived for in-plane field scans, with the external field $\mathbf{H}_0$ much larger than M_s, so that $\mathbf{M} \parallel \mathbf{H}_0$. This is the case in our measurements, since the saturation magnetisation M_s for (Ga,Mn)As and (Ga,Mn)(As,P) is typically a few tens of mT, while the resonance occurs at field of a few hundreds of mT (e.g. see Figure 2d). The bars are approximated to a uniform magnetised sheet. This is a good approximation for the 500 nm and 4 μm samples but in the 80 nm wide bar there is a small contribution to H_U from the in-plane demagnetising field

(calculations shown in Supplementary Information).

1. Vonsovskiĭ, S. V. *Ferromagnetic Resonance* (Pergamon, Oxford, 1966).

2. Tulapurkar, A. A. *et al.* Spin-torque diode effect in magnetic tunnel junctions. *Nature* **438**, 339–342 (2005).

3. Sankey, J. C. *et al.* Spin-transfer-driven ferromagnetic resonance of individual nanomagnets. *Phys. Rev. Lett.* **96**, 227601 (2006).

4. Myers, E. B., Ralph, D. C., Katine, J. A., Louie, R. N. & Buhrman, R. A. Current-induced switching of domains in magnetic multilayer devices. *Science* **285**, 867–870 (1999).

5. Chernyshov, A. *et al.* Evidence for reversible control of magnetization in a ferromagnetic material by means of spin-orbit magnetic field. *Nature Phys.* **5**, 656–659 (2009).

6. Miron, I. M. *et al.* Current-driven spin torque induced by the Rashba effect in a ferromagnetic metal layer. *Nature Mater.* **9**, 230–234 (2010).

7. Aronov, A. G. & Lyanda-Geller, Y. B. Nuclear electric resonance and orientation of carrier spins by an electric field. *JETP Lett.* **50**, 431 (1989).

8. Edelstein, V. Spin polarization of conduction electrons induced by electric current in two-dimensional asymmetric electron systems. *Solid State Commun.* **73**, 233–235 (1990).

9. Inoue, J., Bauer, G. E. W. & Molenkamp, L. W. Diffuse transport and spin accumulation in a Rashba two-dimensional electron gas. *Phys. Rev. B* **67**, 033104 (2003).

10. Silov, A. Y. *et al.* Current-induced spin polarization at a single heterojunction. *Appl. Phys. Lett.* **85**, 5929–5931 (2004).

11. Manchon, A. & Zhang, S. Theory of spin torque due to spin-orbit coupling. *Phys. Rev. B* **79**, 094422 (2009).

12. Garate, I. & MacDonald, A. H. Influence of a transport current on magnetic anisotropy in gyrotropic ferromagnets. *Phys. Rev. B* **88**, 134403 (2009).

13. Costache, M. V., Watts, S. M., Sladkov, M., van der Wal, C. H. & van Wees, B. J. Large cone angle magnetization precession of an individual nanopatterned ferromagnet with dc electrical detection. *Appl. Phys. Lett.* **89**, 232115 (2006).

14. Costache, M. V., Sladkov, M., van der Wal, C. H. & van Wees, B. J. On-chip detection of ferromagnetic resonance of a single submicron Permalloy strip. *Appl. Phys. Lett.* **89**, 192506 (2006).

15. Goennenwein, S. T. B. *et al.* Electrically detected ferromagnetic resonance. *Appl. Phys. Lett.* **90**, 162507 (2007).

16. Mecking, N., Gui, Y. S. & Hu, C.-M. Microwave photovoltage and photoresistance effects in ferromagnetic microstrips. *Phys. Rev. B* **76**, 224430 (2007).

17. Hui, X. *et al.* Electric detection of ferromagnetic resonance in single crystal iron film. *Appl. Phys. Lett.* **93**, 232502 (2008).

18. Yamaguchi, A. *et al.* Broadband ferromagnetic resonance of $Ni_{81}Fe_{19}$ wires using a rectifying effect. *Phys. Rev. B* **78**, 104401 (2008).

19. Silver, M., Batty, W., Ghiti, A. & O'Reilly, E. P. Strain-induced valence-subband splitting in III–V semiconductors. *Phys. Rev. B* **46**, 6781 (1992).

20. Zemen, J., Kučera, J., Olejník, K. & Jungwirth, T. Magnetocrystalline anisotropies in (Ga,Mn)As: Systematic theoretical study and comparison with experiment. *Phys. Rev. B* **80**, 155203 (2009).

21. Rushforth, A. W. *et al.* Molecular beam epitaxy grown (Ga,Mn)(As,P) with perpendicular to plane magnetic easy axis. *J. Appl. Phys.* **104**, 073908 (2008).

22. Hümpfner, S. *et al.* Lithographic engineering of anisotropies in (Ga,Mn)As. *Appl. Phys. Lett.* **90**, 102102 (2007).

23. Wunderlich, J. *et al.* Local control of magnetocrystalline anisotropy in (Ga,Mn)As microdevices: Demonstration in current-induced switching. *Phys. Rev. B* **76**, 054424 (2007).

24. Wenisch, J. *et al.* Control of magnetic anisotropy in (Ga,Mn)As by lithography-induced strain relaxation. *Phys. Rev. Lett.* **99**, 077201 (2007).

25. Hoffmann, F. *et al.* Mapping the magnetic anisotropy in (Ga,Mn)As nanostructures. *Phys. Rev. B* **80**, 054417 (2009).

26. Khazen, K. *et al.* Anisotropic magnetization relaxation in ferromagnetic $Ga_{1-x}Mn_xAs$ thin films. *Phys. Rev. B* **78**, 195210 (2008).

27. Liu, X. & Furdyna, J. K. Ferromagnetic resonance in $Ga_{1-x}Mn_xAs$ dilute magnetic semiconductors. *J. Phys.: Cond. Matt.* **18**, R245– R279 (2006).

Acknowledgements We acknowledge fruitful discussions with Ion Garate, Allan H. MacDonald and Leonid Rokhinson and support from EU Grants FP7-214499 NAMASTE, FP7-215368 SemiSpinNet, ERC Advanced Grant, from Czech Republic Grants AV0Z10100521, KAN400100652, LC510, KJB100100802 and Praemium Academiae, D.F. acknowledges support from Cambridge Overseas Trusts and Hitachi Cambridge Laboratory, A.J.F. acknowledges the support of a Hitachi research fellowship.

Author contribution Device fabrication: D.F., A.J.F.; experiments and data analysis: D.F., H.K., J.W., A.J.F.; theory: K.V., L.P.Z., T.J.; materials: R.P.C., A.C., B.L.G.; writing: D.F., A.J.F., T.J., L.P.Z., K.V., H.K., J.W.; project planning: A.J.F.

Additional information. The authors declare that they have no competing financial interests. Supplementary information accompanies this paper at www.nature.com/naturenanotechnology. Reprints and permission information is available online at http://npg.nature.com/reprintsandpermissions/. Correspondence and requests for materials should be addressed to A.J.F.

Figure captions;

Figure 1, Principle of the experiment and its setup. a, Precession of the magnetisation vector $\mathbf{M}$ around the total magnetic field $\mathbf{H}_{\text{tot}}$. $\mathbf{M}$ is subject to a damping torque τ^{α} due to energy dissipation, which causes the magnetic motion to relax towards $\mathbf{H}_{\text{tot}}$. The driving torque τ^{SO} due to the current-induced effective field counters the effect of damping, and leads to steady-state motion $\partial \mathrm{M}/\partial t = -\gamma \mathbf{M} \times \mathbf{H}_{\text{tot}}$ (grey arrow). The current density vector is represented by $\mathbf{j}(t)$. **b,** SEM image of a 80 nm-wide bar, patterned from the (Ga,Mn)(As,P) wafer. **c,** Schematic of the experimental setup. A microwave frequency current is driven across the nano-scale magnetic bar which is contacted with Cr/Au bondpads. The dc voltage, generated by magnetisation precession, is extracted via a bias tee (represented by the capacitor and inductor network attached between the signal generator and sample source). The dc connection at the drain also provides a microwave ground, represented by a capacitor.

Figure 2, Spin-orbit driven ferromagnetic resonance. a, V_{dc} measured at 8, 10 and 12 GHz (circles) on the 80 nm-wide device. The resonance peaks are clearly observed and can be well-described by the solution to the LLG equation (e.g. Equation 32 in Ref. 16). The solid lines are the fitted results. The difference in the signal level at different frequency is caused by the frequency-dependent attenuation of the microwave circuit. **b,** The resonance field H_{res} as a function of the microwave frequency. The red solid line is the fitted results to Equation 3. **c,** Frequency-dependence of the FMR linewidth ΔH. The data are fitted to a straight line to extract ΔH_{inhomo}

and α. **d,** V_{dc} measured from in-plane rotational scans of the external field $\mathbf{H}_0$. The colour scale represents the magnitude of the voltage. φ is the angle between the magnetisation vector $\mathbf{M}$ and the [100] crystalline axis. **e,** Angle-plot of the resonance field H_{res}. The red line is a fitting curve to Equation 3 and 4 to calculate the magnetic anisotropy.

Figure 3, Characterisation of the driving field in both (Ga,Mn)As and (Ga,Mn)(As,P) devices. a–b, Amplitudes of the anti-symmetric part of the FMR signal V_{asy}, measured on a group of 500 nm-wide (Ga,Mn)As bars, patterned along different crystalline directions. The solid lines are fitted results to Equation 2. **c,** Plot of the magnitude and direction of the current-induced effective field $\mathbf{h}_{\text{eff}}$ measured on the (Ga,Mn)As nano-bars, scaled for a current density $j = 10^5$ A/cm^2. **d,** Similar plot for $\mathbf{h}_{\text{eff}}$ measured on the (Ga,Mn)(As,P) devices. **e–f,** Current density dependence of $\mathbf{h}_{\text{D}}$ and $\mathbf{h}_{\text{R}}$ in both (Ga,Mn)As and (Ga,Mn)(As,P) nano-bars. A second horizontal scale is included for the electric field, calculated from the device resistance (values given in Methods).

Figure 4, SO-FMR on devices patterned from different materials and with various sizes. a, $H_{\text{res}}(\varphi)$ measured from an in-plane rotational scan on a 500 nm-wide (Ga,Mn$_{0.06}$)As bar (patterned along the [010] axis). The circles are measurement data, and the solid line is the fitted result to Equations 3 and 4. **b,** $H_{\text{res}}(\varphi)$ measured on a (Ga,Mn$_{0.06}$)(As,P$_{0.1}$) device with identical shape and orientation. **c,** Comparison of the in-plane anisotropy fields H_i between the two samples. **d,** The linewidth ΔH of the FMR signals measured on the 80 nm, 500 nm and 4 μm (Ga,Mn)(As,P) bars. **e,** Comparison of the magnetic anisotropy (in terms of the profiles of H_{res}) among 80 nm, 500 nm and 4 μm (Ga,Mn)(As,P) bars.

a

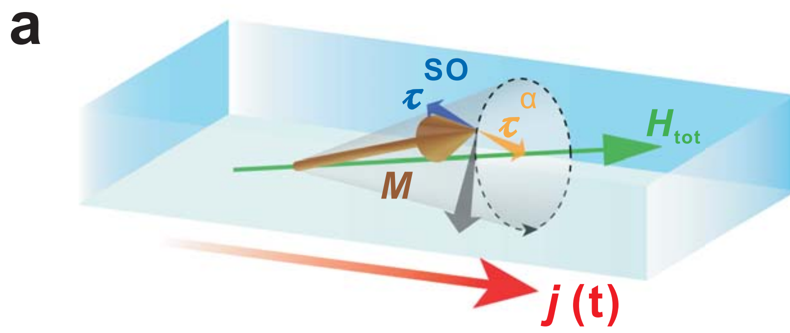

b

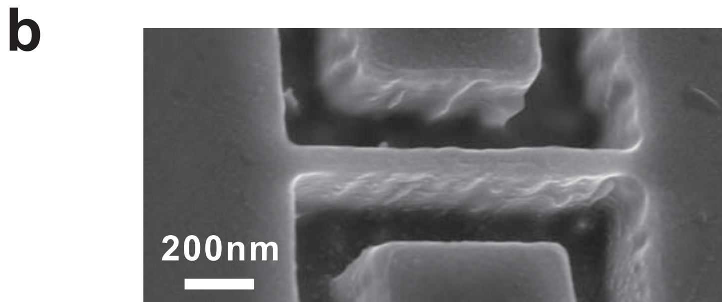

c

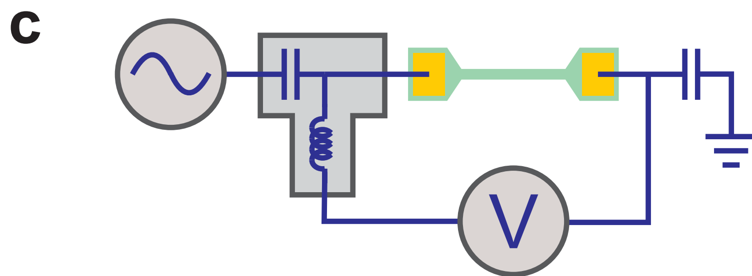

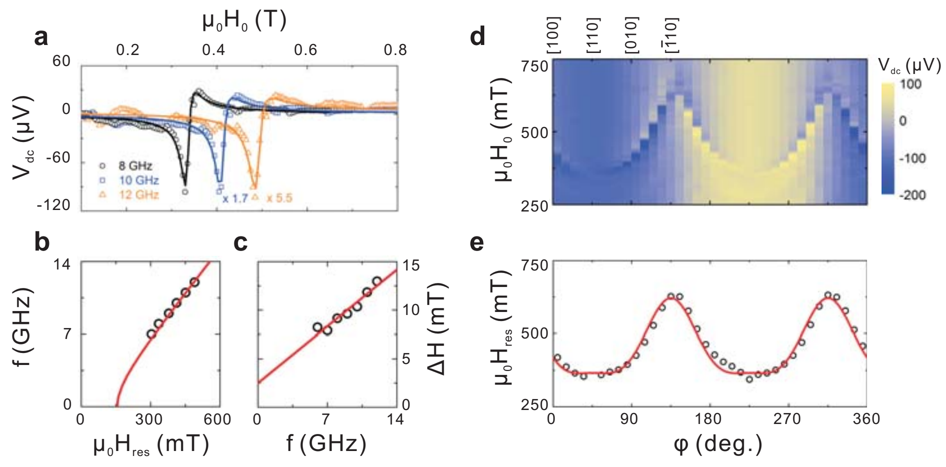
a
μ0H0 (T)
0.2
0.4
0.6
0.8
60
0
-60
-120
Vdc (μV)
8 GHz
10 GHz
12 GHz
x 1.7
x 5.5
b
f (GHz)
14
7
0
0
300
600
μ0Hres (mT)
c
15
10
5
0
ΔH (mT)
0
7
14
f (GHz)
d
[100]
[110]
[010]
[1̄10]
750
500
250
μ0H0 (mT)
Vdc (μV)
100
0
-100
-200
e
750
500
250
μ0Hres (mT)
0
90
180
270
360
φ (deg.)

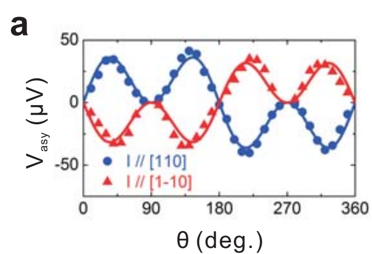
a
V_{asy} (μV)
θ (deg.)
I // [110]
I // [1-10]

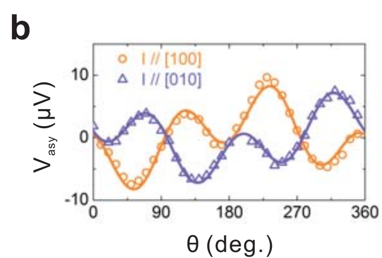
b
V_{asy} (μV)
θ (deg.)
I // [100]
I // [010]

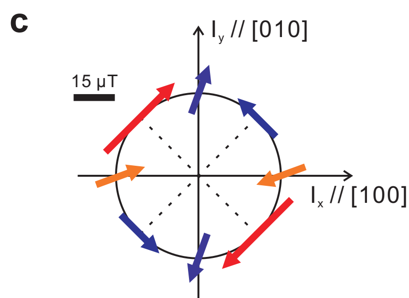
c
I_y // [010]
I_x // [100]
15 μT

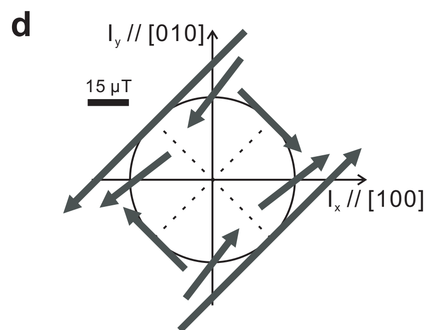
d
I_y // [010]
I_x // [100]
15 μT

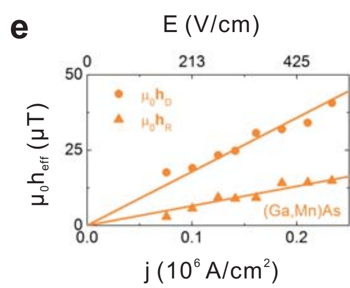
e
E (V/cm)
$\mu_0 h_{eff}$ (μT)
j (10^6 A/cm^2)
$\mu_0 \mathbf{h}_D$
$\mu_0 \mathbf{h}_R$
(Ga,Mn)As

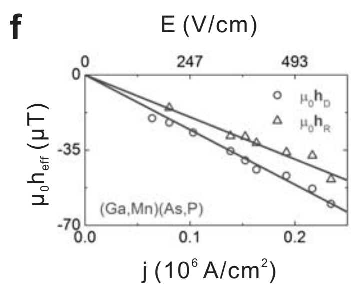
f
E (V/cm)
$\mu_0 h_{eff}$ (μT)
j (10^6 A/cm^2)
$\mu_0 \mathbf{h}_D$
$\mu_0 \mathbf{h}_R$
(Ga,Mn)(As,P)

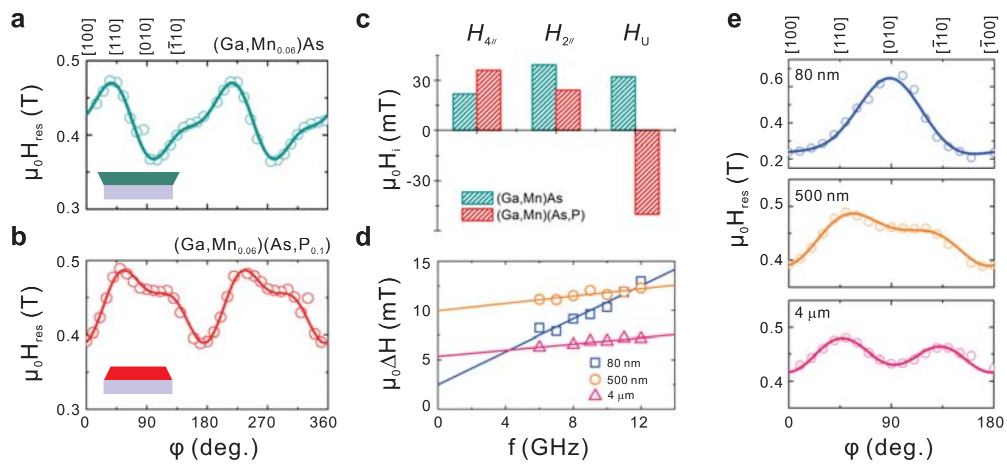
a
[100]
[110]
[010]
[$\bar{1}$10]
(Ga,Mn$_{0.06}$)As
$\mu_0 H_{res}$ (T)
b
(Ga,Mn$_{0.06}$)(As,P$_{0.1}$)
$\mu_0 H_{res}$ (T)
φ (deg.)
c
$H_{4//}$
$H_{2//}$
H_U
$\mu_0 H_i$ (mT)
(Ga,Mn)As
(Ga,Mn)(As,P)
d
$\mu_0 \Delta H$ (mT)
80 nm
500 nm
4 μm
f (GHz)
e
[100]
[110]
[010]
[$\bar{1}$10]
[$\bar{1}$00]
80 nm
500 nm
4 μm
$\mu_0 H_{res}$ (T)
φ (deg.)